



The Microsoft Research - University of Trento
Centre for Computational
and Systems Biology

Technical Report CoSBI 07/2007

Molecular mechanism of energy metabolism in astrocytes: a parametric model from FDG PET images

Paola Lecca

*The Microsoft Research - University of Trento
Centre for Computational and Systems Biology*

lecca@cosbi.eu

Michela Lecca

*Fondazione Bruno Kessler
Center for Information Technology, Trento, Italy*

lecca@fbk.eu

*This is the preliminary version of a paper that will appear in
Advances in Brain, Vision, and Artificial Intelligence, Lecture Notes in Computer Science,
Springer*

available at <http://www.springerlink.com/content/28543x414441760p/>

Molecular mechanism of energy metabolism in astrocytes: a parametric model from FDG PET images

Paola Lecca and Michela Lecca

Abstract

The signals detected during physiological activation of the brain with ^{18}F -deoxyglucose DG PET reflect predominantly uptake of this tracer into astrocytes. This notion provides a cellular and molecular basis for the FDG PET technique. Although in recent years the functional brain imaging has experienced enormous advances, the cellular and, in particular, the molecular mechanisms generating the signals detected by these techniques are not completely known. In this paper, we present a computational model that attempts to disentangle the intricate nature of the molecular interactions governing the brain energy metabolism. The model describes the glutamate-stimulated glucose uptake and use into astrocytes. It consists of a set of ordinary differential equations, each of which specifying the time-behavior of the main molecular species involved in the astrocytic glucose use (i. e. glutamate, glucose, Na^+ , β -threohydroxyaspartate) and the dynamical rates of glutamate, glucose and Na^+ uptake. The kinetic rates constants of the model have been identified on a set of dynamic PET images. As far as we know, a mathematical and computational model of the brain energy metabolism at the molecular level has been never proposed. The relevance of such a model to the PET functional brain imaging consists in providing an *in silico* framework, in which to experiment the molecular glucose dynamics and elucidate their still elusive aspects.

1 Introduction

Positron Emission Tomography, also called PET imaging or PET scan is both a medical and research used to detect blood flow, oxygen consumption and energy metabolism. It consists in the acquisition of physiologic images based on the detection of radiation from the emission of positrons. To conduct the scan, a short-lived radioactive tracer isotope, that decays by emitting positrons, is chemically incorporated into a metabolically active molecule. Most commonly, this molecule is the fluorodeoxyglucose (FDG). Then the radioactive tracer attached to the metabolic molecule is injected into the blood circulation of the patient. After a waiting period time that the active metabolite needs to concentrate in the tissues, the patient is placed in the imaging scanner. The changing of regional blood flow in various anatomic structures as a measure of the injected positron emitter can be visualized and quantified with a PET scan. FDG-PET is widely used in clinical oncology, but is also an important research tool to map brain functions, since it is capable of detecting areas of molecular biology detail even prior to anatomic change. The kinetics of the FDG tracers are similar to glucose. It passes through the brain-blood barrier and is phosphorylated intracellularly in a process analogous to the glucose. The phosphorylated FDG compound does not enter in the Krebs cycle, thence it is effectively trapped.

Despite the striking advances in PET functional brain imaging [5, 10], the molecular mechanisms that underlie the signals detected by this technique are still largely unknown. The basic physiological principle is represented by the tight coupling between neuronal activity and the associated increase in both blood flow and glucose metabolism. The development of the autoradiographic 2-deoxyglucose method by Sokoloff about 30 years ago, proved the coupling between synaptic activity and glucose use, the so-called neurometabolic coupling [11, 12]. Wet experimental analyses *in vitro* have been carried out to investigate the neurotransmitter-regulated metabolic fluxes and to determine the cellular localization of enzymes and transporters involved in the glucose metabolism. At the same time *in vivo* approaches, as microdialysis and magnetic resonance approaches have recognized in the neurotransmitter glutamate and astrocytes, a specific type of glial cells, the key elements in the coupling between the synaptic activity and the glucose metabolism (for a detailed review about recent and less recent studies see [6]). Nevertheless, many aspects of the molecular interactions driving the glucose uptake and consumption are still elusive. In this article we present a mathematical model of the glutamate-triggered glucose uptake and metabolism by focusing on the emerging central role of the reaction occurring within astrocytes. At the best of our knowledge, this work is the first to provide a computational model related to the molecular basis of the use of the glucose in astrocytes. Our model consists of a set of seven differ-

ential equations, describing the time behavior of the glutamate and glucose use into the astrocyte. The synaptically released glutamate triggers glucose flux in astrocytes. The time course model of the glucose concentration inside that glial cell is related to the concurrency of the inhibitory action of the β -threohydroxyaspartate on the glutamate-stimulated glucose use and the activity of the Na^+/K^+ -ATPase. The latter stimulates glucose uptake and glycolysis. The simulation parameters of the model, as the initial concentration of the reactants molecules and the kinetic rate constants, have been estimated by a slice-by-slice fit of the data of 31 PET-scans, each of which consisting of 15 horizontal slices, of a brain of a normal subject. The shapes of the brain activity curves, obtained by solving the equations, show a behavioral agreement with the typical measured blood activity curves of normal subjects [14]. Moreover, the results of our model simulations are in agreement with the simulations of the Sokoloff's model describing the kinetics of the compound FDG. This last fact, in particular, validates our model further on, since it is an additional confirmation that the model includes the most salient features of the molecular machinery of the astrocytic glucose metabolism. Finally, with respect to the model presented in this paper, the Sokoloff's model can be considered as a *black box* approach to the glucose metabolism kinetics, that Sokoloff indirectly obtained from the kinetics of the FDG tracer.

2 Glucose use in astrocytes

Astrocytes are sub-type of the glial cells in the brain. Following a group of recent studies, researchers have found an increasing amount of evidence that suggests that the astrocytes play a central role in brain function by affecting the activity of neurons, by taking an active part in the distribution of energy substrates from the circulation to neurons [15, 16]. The ratio between neuronal and non-neuronal cells depends on species, brain areas or developmental ages, it is a well-established fact that neurons contribute at most 50% of cerebral cortical volume [2] and that the astrocytes outnumber the neurons ten to one.

Astrocytes are stellate cells (hence their name) with multiple fine processes, some of which are in close apposition to capillary walls. The entire surface of intraparenchymal capillaries is covered by these specialized processes, called astrocytic end-feet. This cytoarchitectural arrangement implies that astrocytes form the first cellular barrier encountered by the glucose entering the brain parenchyma. Therefore astrocytes are a likely site of prevalent glucose uptake. The uptake of glucose in astrocyte is triggered by glutamate. The glutamate is the main excitatory neurotransmitter of the cerebral cortex. Activation of afferent pathways by specific modalities (e. g. visual, auditory, somatosensory) results in a spatially and temporally

defined local release of glutamate from the activated specific synapses. The action of glutamate on postsynaptic neurons terminates with the reuptake of glutamate in astrocytes [1, 3, 4].

Glutamate uptake into astrocytes is driven by the electro-chemical gradient of Na^+ ; it is an Na^+ -dependent mechanism with a stoichiometry of three Na^+ ions cotransported with one glutamate molecule. A consequence of the glutamate uptake into astrocytes is the stimulation of glucose uptake and aerobic glycolysis in these cells, i. e. of glucose use [8]. Glutamate-stimulated increase in glucose uptake into astrocytes is abolished in the absence of Na^+ in the extracellular medium, consistently with the necessity for an electro-chemical gradient for the ion to drive glutamate uptake. A central role in the coupling between glutamate transporter activity and glucose uptake into the astrocytes is the activation of the Na^+/K^+ -ATPase. The astrocytic Na^+/K^+ -ATPase responds to increases in intracellular Na^+ concentration. Well established experimental observations [9] show that glutamate activates Na^+/K^+ -ATPase. There is also an ample evidence from studies in a variety of cellular systems including brain, kidney, vascular smooth muscle and erythrocytes, that increases in the activity of the Na^+/K^+ -ATPase stimulates glucose uptake and glycolysis [8]. Finally, the specific glutamate transporter inhibitor β -threohydroxyaspartate inhibits the glutamate-stimulate glucose use [6, 8]. Figure 1 depicts the mechanism of glucose absorption and use inside the astrocyte.

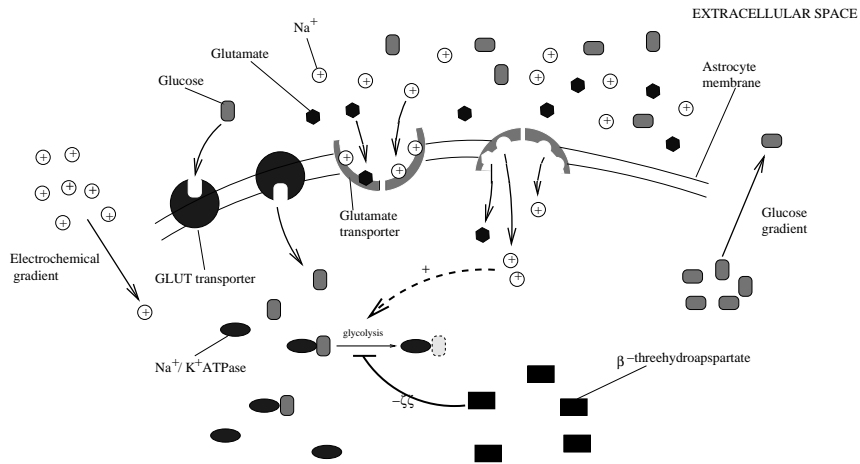


Figure 1: A diagram of the reactions governing the astrocytic glycolysis.

3 The kinetic model

The rate equation of the concentration of glucose in the astrocyte ($GLUCOSE_{IN}$) is composed by three terms (Eq. (1)). The first term models the glutamate-

stimulated glucose increase as a direct proportionally between the time derivative of glucose astrocytic concentration and the glutamate astrocytic concentration (*GLUTAM*). The second term is the product of the rate of glucose uptake and its astrocytic concentration. This term expresses the proportionality between the time change of astrocytic glucose and both the flux of incoming glucose (*GL_{IN}*) and the glucose astrocytic concentration. Finally, the third term in Eq. (1) represents the decrease of glucose in astrocyte due to the Na⁺/K⁺-ATPase - stimulated glycolysis. Since the astrocytic Na⁺/K⁺-ATPase is activated by glutamate in response to increases in intracellular Na⁺ concentration, the rate equation for Na⁺/K⁺-ATPase (Eq. (3)) is given by a term proportional to the concentration of Na⁺ in the astrocyte and by a negative term proportional to the amounts of β-threohydroxyaspartate and Na⁺/K⁺-ATPase. This term models the inhibition of glutamate-stimulated glucose use performed by β-threohydroxyaspartate. In Eq. (3) the inhibition of glycolysis is modeled by a decrement term in the rate equation of Na⁺/K⁺-ATPase. In fact a decrement of the amount of this enzyme causes a decrement of the glycolytic events.

$$\begin{aligned} &\textbf{Glucose entering into the astrocyte} && (1) \\ &\frac{dGLUCOSE_{IN}}{dt} = k_1 GLUTAM + k_2 GL_{IN} \cdot GLUCOSE_{IN} - k_3 NA_K_ATPase \cdot GLUCOSE_{IN} \end{aligned}$$

$$\begin{aligned} &\textbf{Glutamate entering into the astrocyte} && (2) \\ &\frac{dGLUTAM}{dt} = k_4 GT_{IN} \cdot GLUTAM \end{aligned}$$

$$\begin{aligned} &\textbf{Na⁺ K⁺ ATPase} && (3) \\ &\frac{dNA_K_ATPase}{dt} = k_5 NA_{IN} - k_6 GT_INHIBIT \cdot NA_K_ATPase \end{aligned}$$

$$\begin{aligned} &\textbf{β-threohydroxyaspartate} && (4) \\ &\frac{dGT_INHIBIT}{dt} = -k_7 NA_{IN} \cdot GT_INHIBIT \end{aligned}$$

$$\begin{aligned} &\textbf{Rate of glucose uptake into the astrocyte} && (5) \\ &\frac{dGL_{IN}}{dt} = k_8 GLUT_{OPEN} \cdot GL_{IN} \end{aligned}$$

$$\begin{aligned} &\textbf{Rate of glutamate uptake into astrocyte} && (6) \\ &\frac{dGT_{IN}}{dt} = (k_9 GLT_1 + k_{10} GLAST)GT_{IN} + k_{11} (NA_{IN} - NA_{OUT}) \end{aligned}$$

$$\begin{aligned} &\textbf{Na⁺ uptake into astrocyte} && (7) \\ &\frac{dNA_{IN}}{dt} = k_{12} GLUTAM \end{aligned}$$

(8)

The rate equation for the astrocytic glutamate concentration (Eq. (2))

is the product of the glutamate amount in the cell and the flux of incoming glutamate (GT_{IN}). The fluxes of glutamate and glucose entering the astrocyte (GL_{IN} and GT_{IN} , respectively) have been modeled as functions of time. Experimentally the rate at which glucose is transported into the cell is determined by the rate at which the concentration of glucose accumulates inside the cell in the absence of metabolism [7]. Thence, the temporal derivatives of the glucose and glutamate fluxes are given by Eq. (5) and Eq. (6) respectively. Eq. (5) contains a term accounting for the number of GLUT transporter in an open state ($GLUT_{OPEN}$), i. e. transporters that are facing the exterior of the cell and ready to receive a glucose molecule. Similarly, Eq. (6) contains a term proportional to the fraction of two types of glutamate transporters GLT_1 and $GLAST$ and a term proportional to the difference between the internal and external concentration of Na^+ (NA_{IN} and NA_{OUT} , respectively).

Eq. (4) is the rate equation for the β -threohydroxyaspartate. The time derivative of this inhibitor is given by the product of the concentration of β -threohydroxyaspartate itself and the concentration of Na^+ . Namely, since the inhibitory activity of the β -threohydroxyaspartate is consequent to the increase of the concentration of Na^+ , that in turn is also responsible for the activation of the glycolytic activity of Na^+/K^+ -ATPase.

Finally, Eq. (7) describes the time behavior of the astrocytic concentration of Na^+ . Its time derivative is proportional to the astrocytic concentration of glutamate. This equation expresses the direct relationship between glutamate and the cotransported Na^+ . The coupling between synaptic glutamate release and its re-uptake into astrocyte is so tight that the determination of the Na^+ current generated in astrocytes by the co-transport of glutamate and Na^+ through the glutamate transporters provides an accurate estimate of glutamate release from the synapses [1].

3.1 PET image processing and parameters derivation

The dynamic FDG PET data used in this work have been provided by the Neurobiology Research Group, Rigshospitalet, Copenhagen. These data consist of 31 three-dimensional grey level images of the brain of a normal subject. The scans have been taken with a Scanditronix 4096 scanner on a time range of 3429 seconds. Figure 2 shows a set of brain slices of the data base used in this work.

To identify the kinetic rates ks of the model we used a standard fit procedure of the time-dependency of glucose concentration obtained from the PET images. For the fit we used a simple least squares cost function. Before obtaining the measured time-dependence of glucose concentration, the images have been processed in order to eliminate noise and border effects and identify exclusively the region corresponding to the brain. The identification

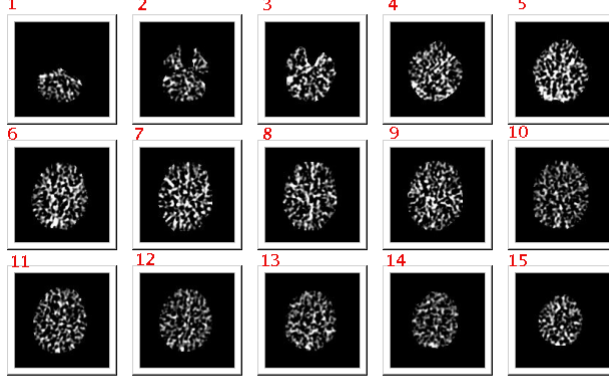


Figure 2: A view of a set of brain slices.

of the brain region and the elimination of the noisy parts on the borders of the skull have been performed with the following procedure. Let I_j denote the 3D-scan taken at time t_j and $\{I_j^1, \dots, I_j^{15}\}$ with $j = 1, \dots, 31$, the set of 15 slices of the j -th scan. For each scan I_j and for each slice I_j^k ($k = 1, \dots, 15$), we calculated the smallest polygon P_j^k , enclosing the pixels, whose grey-level is greater than zero (i. e. the pixels which do not belong to the background). The boundary of this polygon has been smoothed by a simple procedure of elimination of its parts having thickness larger than one pixel. Hence, for each slice I_j^k , the region R_j^k , we estimated as region effectively corresponding to the brain, is given by the topological internal part of P_j^k and the P_j^k boundary itself (see Figure 3 related to slice 7 and the figures in Appendix B related to the other slices). Moreover, we defined

$$R_k \equiv \cup_{h=1}^{31} R_h^k, \quad k = 1, \dots, 15$$

and we calculated the glucose concentration variation slice by slice using the following formula

$$\frac{dG_k}{dt}(t_i) = \frac{1}{\text{Area}(R_k)} \sum_{p \in R_k} \frac{|\sigma_p(t_i) - \sigma_p(t_{i+1})|}{t_{i+1} - t_i} \quad (9)$$

where $\sigma_p(t_i)$ is the intensity of the pixel $p \in R_k$ at time t_i ($i = 1, \dots, 31$).

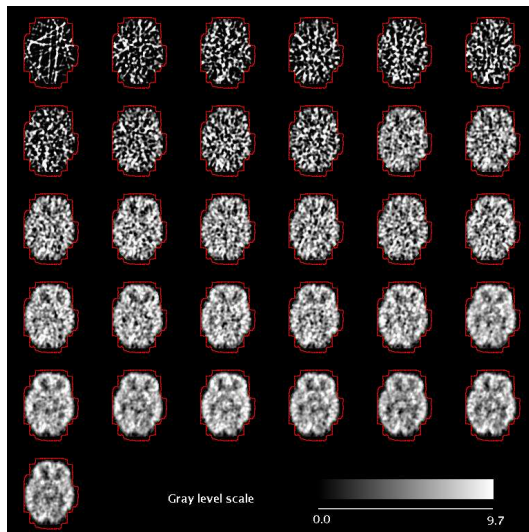


Figure 3: The red boundary encloses the regions R_j^k for $j = 1, \dots, 31$ and $k = 7$. The value on the grey level scale are measured in Bq/cc.

Two kinds of analyses has been carried out pixel by pixel to reveal a possible partitioning of the brain slice in activation areas:

- For each slice I_j^k of an image I_j we defined a *frequency map* M of pixel activation in the following way

$$M : R_k \longrightarrow \mathbb{N}$$

$$M[p] = \begin{cases} 0 & \text{if } p \notin R_k \\ m & \text{otherwise} \end{cases}$$

where m is the number of intensity's changes occurred in pixel p .

This analysis showed that almost all the pixels exhibit the same frequency of intensity's change.

- We also computed pixel by pixel for each slice of each scan the average glucose variation to detect possible clusters of pixels characterized by different levels of changes in glucose concentration variation. Also this kind of analysis showed that the time changes in glucose contrition are homogeneously distributed.

The set of figures in Appendix B shows a homogeneous distribution of pixels of any intensity.

The only spatial partitioning detectable in our data set consists in two set of images: *set 1* consisting of the 31 scans of the brain slice 1 and 2, and

set 2 containing the 31 scans of the remaining 14 slices (from 3 to 15). The numeration of the slices refer to the one given in Figure 2. This partitioning is pointed out by the different rate, with which the glucose concentration changes over time. Figures 4 a. and b. show the time behavior of glucose concentration for the slices of set 1 and set 2, respectively. In table 1 the values of the initial concentrations of the reactants and the kinetic rates constants are shown. Figure 5 shows the model simulation of time-dependent glucose concentration for the slices of set 1.

Species	Initial concentration ($\times 0.0379016$ Bq/cc)
<i>GLUCOSE_{IN}</i>	12.00
<i>GLUTAMATE_{IN}</i>	11.00
<i>NA_K_ATPase</i>	2.0
<i>GT_INHIBIT</i>	0.01
<i>GL_{IN}</i>	0.10
<i>GT_{IN}</i>	0.10
<i>NA_{IN}</i>	0.70
Constants	Values
<i>NA_{OUT}</i>	0.1
<i>GLUT_{OPEN}</i>	0.1
<i>GLT_1</i>	0.1
<i>GLAST</i>	0.1

Rate	Value (sec^{-1})	
	Set 1	Set 2
k_1	0.0003	0.0100
k_2	0.0003	0.0500
k_3	0.0100	0.1000
k_4	0.0100	0.3000
k_5	0.1000	0.2000
k_6	0.0800	0.0800
k_7	0.1000	0.0300
k_8	0.0100	0.0500
k_9	0.1000	0.1000
k_{10}	0.1000	0.2000
k_{11}	0.1000	10.000
k_{12}	0.1000	0.1000

Table 1: Space parameter of the model

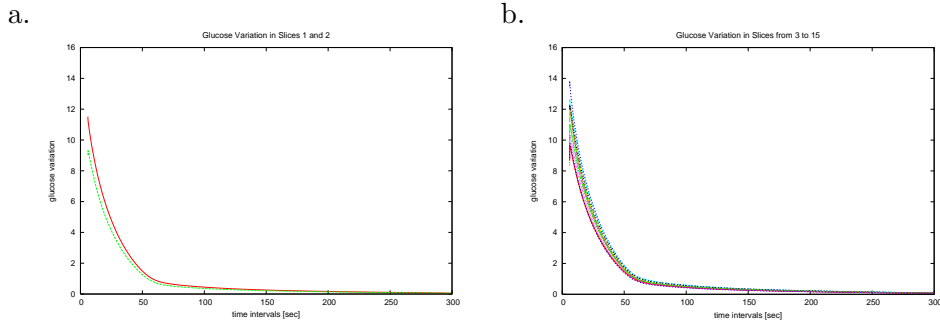


Figure 4: **a.** Time behavior of glucose concentration in brain slice 1 and slice 2. The values on y -axis express are measured in $0.0379016 \times \text{Bq/cc}$. **b.** Time behavior of glucose concentration for slices 3-15. The values on y -axis express are measured in $0.0379016 \times \text{Bq/cc}$.

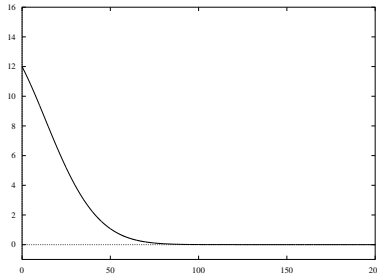


Figure 5: Numerical solution of the model for the kinetic parameters of set 1. On y -axis the glucose concentration is plotted, whereas the x -axis reports the time in seconds.

4 Conclusions and future directions

Functional neuroimaging techniques such as PET have provided valuable insights into the working brain. However, fundamental questions related to the cellular and molecular aspects of neurometabolic coupling are unresolved. Moreover different PET studies provide discordant results about glycolytic metabolism, that in general are related to methodological issues and different simulation protocols. Our computational model describes the molecular origin of the neurometabolic coupling and provides also a theoretical framework to understand and experiment the glucose metabolism by tuning the initial conditions and rate parameters. The model simulations, performed with the kinetic parameters derived from the PET images, are consistent with the blood activity curves observed in the PET studies on normal subjects [14]. The data used in this work to derive the kinetic rate constants do not reveal an evident spatial partitioning of the brain slice in specific activation areas, as in the studies in [14]. The difference, we de-

tected, between the values of the kinetic rates of the two sets of slices may suggest different explanatory hypotheses, such as differences in astrocytic spatial distribution and metabolism in different slices in the brain of the subject considered in this studies. Future advances in our work will consist in the development of methods to model the noise in the PET image in order to obtain less noisy blood activity curves and consequently more accurate estimates of the rate parameters. Moreover the study will be extended to a data set of subjects engaged in specific activities. In this case, by fitting our molecular model to these kind of data it may be possible to individuate regional sets of kinetic rates accurately corresponding to brain activation areas.

Acknowledgements

The authors thank Claus Svarer of Neurobiology Research Unit, Copenhagen University Hospital Rigshospitalet. Claus kindly provided the PET data used in this work.

References

- [1] D. E. Bergles and C. E. Jahr, Glials contribution to glutamate uptake at Schaffer collateral-commissural synapses in the hippocampus. *J. Neurosci*, vol. 18, pp. 7709-7716, 1998.
- [2] A. Bignami, Glial cells in the central nervous system. *Discussions in neuroscience*, vol. 8, no. 1, pp. 1-45, 1991.
- [3] L. Hertz, L. Peng and G. A. Dienel, Energy metabolism in astrocytes: high rate of oxidative metabolism and spatiotemporal dependence on glycolysis/glycogenolysis, *J. of Cerebral Blood Flow & metabolism*, vol. 27, pp. 219-249, 2007
- [4] K. A. Kasiscke, H. D. Vishwasrao, P. J. Fisher, W. R. Zipfel and W. W. Webb, Neuronal activity triggers neuronal oxidative metabolism followed by astrocytic glycolysis, *Science*, vol.305, no. 5680, pp. 99-103, July 2004.
- [5] Y. Kimura, Y. Takabayashi, K. Oda, K. Ishii and K. Ishiwata, Functional image on glucose metabolism in brain using PET with short time scan, In *Procs of the 25th Annual International Conference of the IEEE EMBS*, Cancun, Mexico 2003.
- [6] P. J. Magistretti and L. Pellerin, Cellular mechanisms of brain energy metabolism and their relevance to functional brain imaging., *Phil. Trans. R. Soc. Lond. B*, vol. 354, pp. 1155-1163, 1999.

- [7] E. S. Marland and J. E. Keizer, Transporters and Pumps, Chapter 3 of Computational Cell Biology C. P. Fall, E. S. Marland, J. M. Wagner and J. J. Tyson Editors, Springer-Verlag 2000.
- [8] L. Pellerin and P. J. Magistretti, Glutamate uptake into astrocytes stimulates aerobic glycolysis: a mechanism coupling neuronal activity to glucose utilization, Proc. Natl. Acad. Sci., vol. 91, pp. 10625-10628, 1994.
- [9] L. Pellerin and P. J. Magistretti, Glutamate uptake stimulates Na^+/K^+ -ATPase activity in astrocytes via an activation of the Na^+/K^+ -ATPase, J. Neurochem. vol69, pp. 2132-2137.
- [10] R. G. Shulman, *Functional imaging studies: linking mind and basic neuroscience*, Am. J. of Psychiatry, 2001.
- [11] L. Sokoloff, M. Reivich, C. Kennedy, M. H: des Rosiers, C. S. Patlak, K. D. Pettigrew, O. Sakurada and M. Shinoara, *The ^{14}C deoxyglucose method for the measurement of local cerebral glucose utilization: theory, procedure, and normal values in the conscious and anesthetized albino rat.*, J. of Neurochem., vol. 26, pp. 897-916, 1977.
- [12] L. Sokoloff, Relationship between functional activity and energy metabolism in the nervous system: whether, where and why? In Brain work and mental activity (ed. N. A. Lassen, D. H. Ingvar, M. E. Raichle and L. Friberg), pp. 52-64 Copenhagen: Munksgaard, 1991.
- [13] L. Sokoloff, Energetics of functional activation in neural tissues. Neurochem. Res. vol. 24, pp. 321-329, 1999.
- [14] C. Svarer, I. Iaw, S. Holm, N. Mørch and O. Paulson, Estimation of the glucose metabolism from dynamic PET-scan using neural networks (available at citeseer.ist.psu.edu/227145.html), 1995.
- [15] T. Takano, G. F. Tian, W. Peng, N. Lou, W. Libionka, X. Han and M. Nedergaard, astrocytes mediated control of cerebral blood flow, Nat. Neurosci. vol. 9, p. 260-267, 2006.
- [16] A. Volterra and J. Meldolesi, Astrocytes, from brain glue to communication: the revolution continues, Nat. rev. Neurosci, no.6 pp. 626-640, 2005.

A Appendix

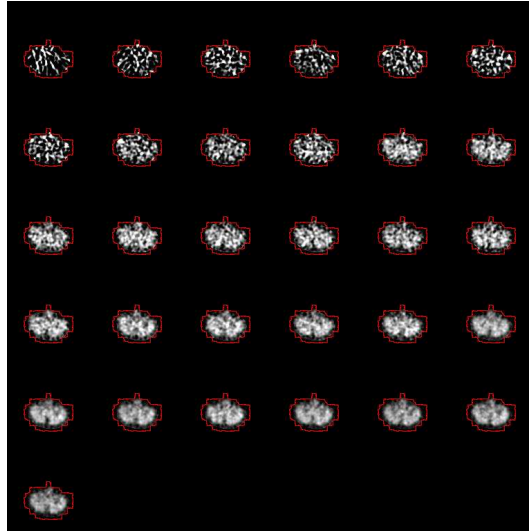


Figure 6: Sets of scans of slice 1. The red boundary encloses the regions R_j^k for $j = 1, \dots, 31$ and $k = 1$. The value on the grey level scale are measured in Bq/cc.

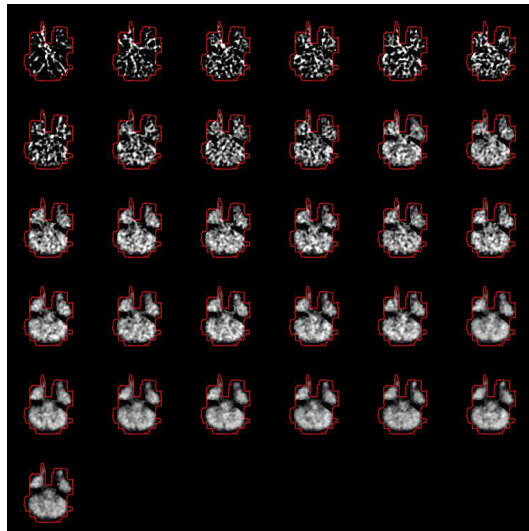


Figure 7: Sets of scans of slice 2. The red boundary encloses the regions R_j^k for $j = 1, \dots, 31$ and $k = 2$. The value on the grey level scale are measured in Bq/cc.

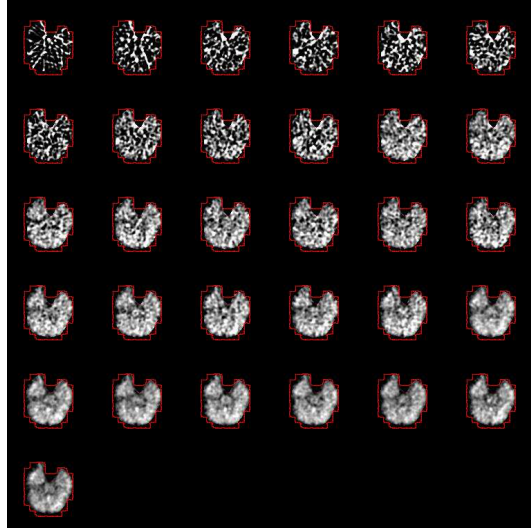


Figure 8: Sets of scans of slice 3. The red boundary encloses the regions R_j^k for $j = 1, \dots, 31$ and $k = 3$. The value on the grey level scale are measured in Bq/cc.

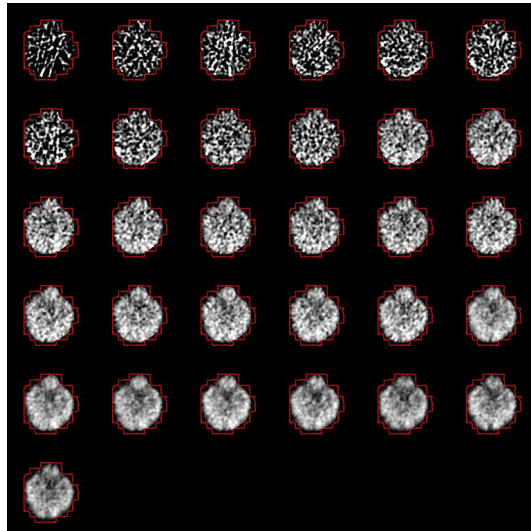


Figure 9: Sets of scans of slice 4. The red boundary encloses the regions R_j^k for $j = 1, \dots, 31$ and $k = 4$. The value on the grey level scale are measured in Bq/cc.

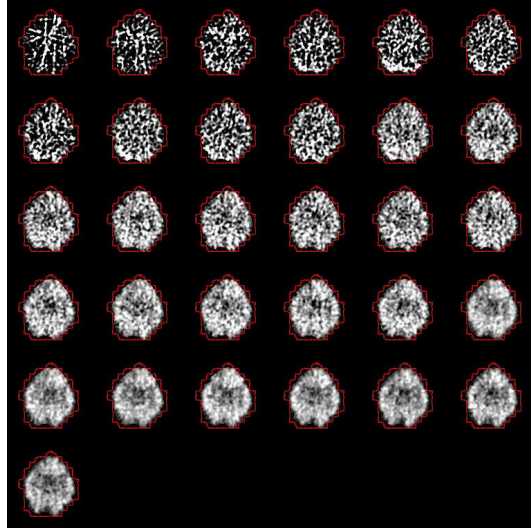


Figure 10: Sets of scans of slice 5. The red boundary encloses the regions R_j^k for $j = 1, \dots, 31$ and $k = 5$. The value on the grey level scale are measured in Bq/cc.

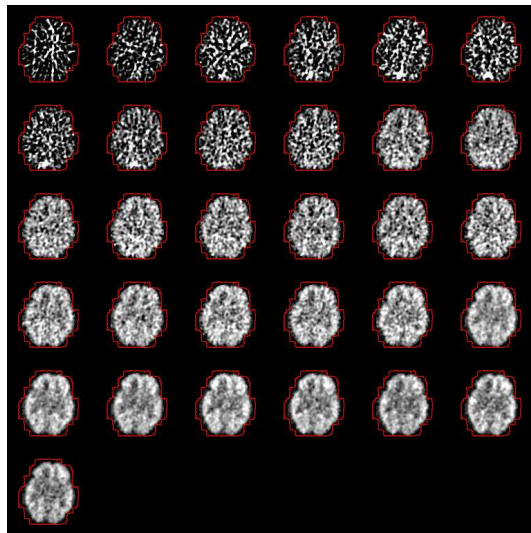


Figure 11: Sets of scans of slice 6. The red boundary encloses the regions R_j^k for $j = 1, \dots, 31$ and $k = 6$. The value on the grey level scale are measured in Bq/cc.

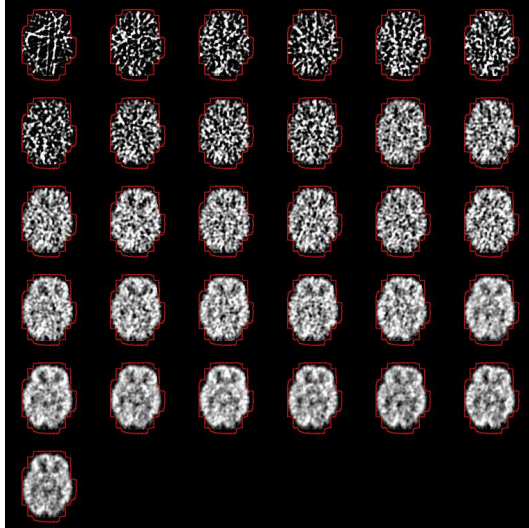


Figure 12: Sets of scans of slice 7. The red boundary encloses the regions R_j^k for $j = 1, \dots, 31$ and $k = 7$. The value on the grey level scale are measured in Bq/cc.

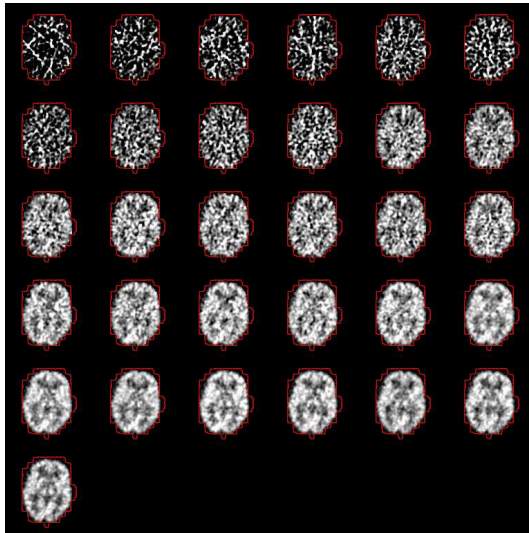


Figure 13: Sets of scans of slice 8. The red boundary encloses the regions R_j^k for $j = 1, \dots, 31$ and $k = 8$. The value on the grey level scale are measured in Bq/cc.

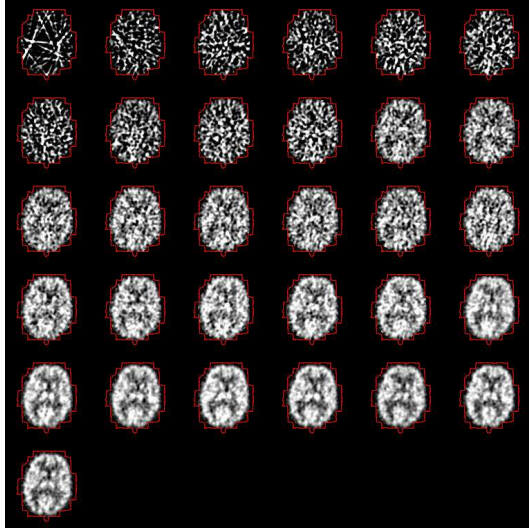


Figure 14: Sets of scans of slice 9. The red boundary encloses the regions R_j^k for $j = 1, \dots, 31$ and $k = 9$. The value on the grey level scale are measured in Bq/cc.

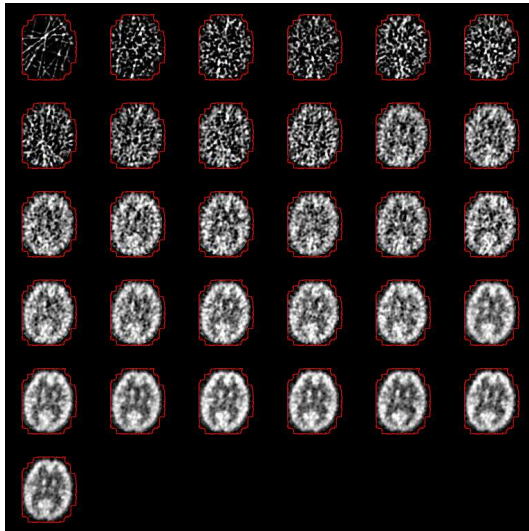


Figure 15: Sets of scans of slice 10. The red boundary encloses the regions R_j^k for $j = 1, \dots, 31$ and $k = 10$. The value on the grey level scale are measured in Bq/cc.

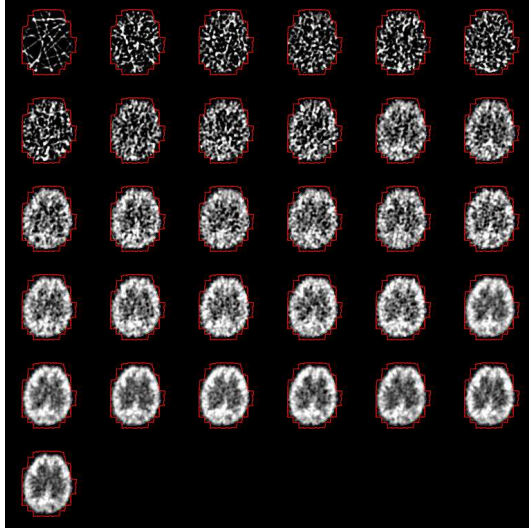


Figure 16: Sets of scans of slice 11. The red boundary encloses the regions R_j^k for $j = 1, \dots, 31$ and $k = 11$. The value on the grey level scale are measured in Bq/cc.

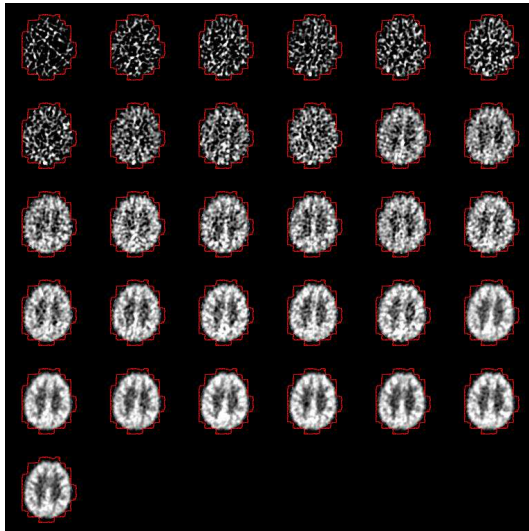


Figure 17: Sets of scans of slice 12. The red boundary encloses the regions R_j^k for $j = 1, \dots, 31$ and $k = 12$. The value on the grey level scale are measured in Bq/cc.

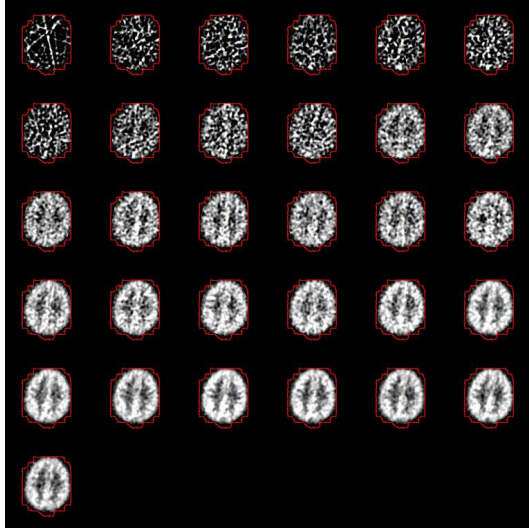


Figure 18: Sets of scans of slice 13. The red boundary encloses the regions R_j^k for $j = 1, \dots, 31$ and $k = 13$. The value on the grey level scale are measured in Bq/cc.

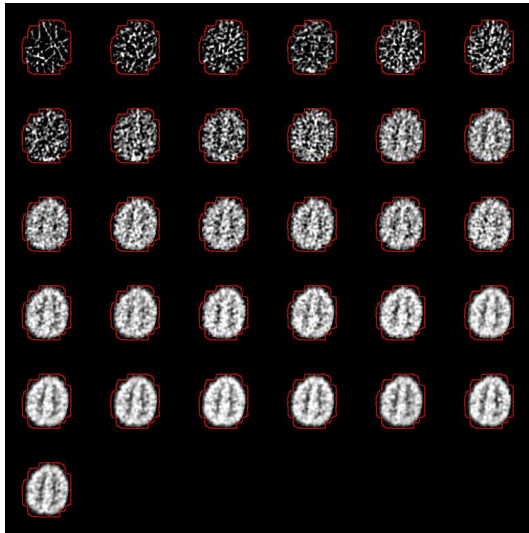


Figure 19: Sets of scans of slice 14. The red boundary encloses the regions R_j^k for $j = 1, \dots, 31$ and $k = 14$. The value on the grey level scale are measured in Bq/cc.

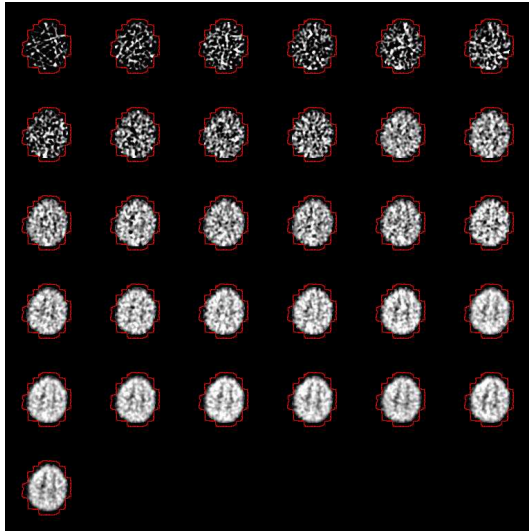


Figure 20: Sets of scans of slice 15. The red boundary encloses the regions R_j^k for $j = 1, \dots, 31$ and $k = 15$. The value on the grey level scale are measured in Bq/cc.